Locations of boundaries of outer and inner radiation belts as observed by Cluster and Double Star

N. Yu Ganushkina,[1,2] I. Dandouras,[3] Y. Y. Shprits,[4] and J. Cao[5,6]

Received 14 December 2010; revised 14 June 2011; accepted 29 June 2011; published 28 September 2011.

[1] Cluster CIS ion spectrograms measured during the period of the recent solar minimum between April 2007 and June 2009, when Cluster was deep in the radiation belts with its perigee as close as L = 2, are analyzed. The analysis is complemented by Double Star TC-1 satellite data from HIA ion spectrograms on perigee passes during the period of May 15, 2007 to September 28, 2007. We demonstrate how the background counts produced by energetic particles of the radiation belts in Cluster CIS and Double Star HIA instruments can be interpreted to obtain the locations of the boundaries of the outer and inner belts. The obtained L-MLT distribution of boundaries reflects the general structure of the radiation belts. Closer examination of the time-dependent L locations of the boundaries reveals several dips to lower L-shells (from L = 6 to L = 4) in the outer boundary location. The importance of the solar wind pressure increases for the Earthward shift of the outer boundary of the outer belt is discussed. The location and thickness of the slot region are studied using the determined inner boundaries of the outer belt and the outer boundaries of the inner belt. It was found that during intervals of low activity in the solar wind parameters, the slot region widens, which is consistent with weaker inward radial diffusion, and also with weaker local acceleration that can occur only at higher L-shells outside the plasmasphere. We conclude that boundaries of radiation belts determined from background measurements on the instruments with energy ranges that do not cover the radiation belts' energies provide valuable additional information that is useful for radiation belts' model development and validation.

Citation: Ganushkina, N. Y., I. Dandouras, Y. Y. Shprits, and J. Cao (2011), Locations of boundaries of outer and inner radiation belts as observed by Cluster and Double Star, *J. Geophys. Res.*, *116*, A09234, doi:10.1029/2010JA016376.

1. Introduction

[2] The Earth's radiation belts consist of energetic electrons and protons trapped by the Earth's magnetic field. Protons form one radiation belt, while electrons exhibit a two zone structure. The inner electron belt is located typically between 1.2 and 3 R_E, while the outer belt extends from about 3 to 7 R_E. The inner electron belt is rather stable and is formed by a slow inward radial diffusion influenced by losses due to Coulomb scattering and to whistler mode pitch angle diffusion [*Lyons and Thorne*, 1973; *Abel and Thorne*, 1998; *Boscher and Bourdarie*, 2001]. The radiation belt electron fluxes in the outer belt are highly dynamic and show variations both in space and time, especially during geomagnetically active times. The observed variability is due to the competing source and loss processes [*Reeves et al.*, 2003], both of which are driven by solar dynamics [e.g., *Shprits et al.*, 2008a, 2008b].

[3] The slot region is located at approximately $2 < L < 3$, separating the inner and outer belts. It is generally known that the radiation belt slot region is formed because energetic electrons are lost due to enhanced pitch angle scattering by VLF waves, mainly whistler waves associated with plasmaspheric hiss emission [*Lyons and Thorne*, 1973; *Lyons and Williams*, 1984; *Imhof et al.*, 1982]. Many studies have focused on the origin and distribution of these waves [*Thorne et al.*, 1974; *Abel and Thorne*, 1998; *Imhof et al.*, 1986; *Green et al.*, 2005]. During the main phase of a storm, the electron slot region may disappear [e.g., *Thorne et al.*, 2007]. The slot then recovers after the storm, typically a few days into the recovery.

[4] The response of the magnetosphere to solar variability is still poorly understood. *Reeves et al.* [2003] showed that, compared to pre-storm conditions, approximately half of all geomagnetic storms result in a net depletion of the outer radiation belt [*Onsager et al.*, 2002; *O'Brien et al.*, 2001] or

[1]Finnish Meteorological Institute, Helsinki, Finland.
[2]Department of Atmospheric, Oceanic and Space Sciences, University of Michigan, Ann Arbor, Michigan, USA.
[3]IRAP, UPS-OMP, University of Toulouse, CNRS, Toulouse, France.
[4]Institute of Geophysics and Planetary Physics, Department of Atmospheric and Oceanic Sciences, University of California, Los Angeles, California, USA.
[5]State Key Laboratory of Space Weather, CSSAR, CAS, Beijing, China.
[6]School of Astronautics, Beijing University of Aeronautics and Astronautics, Beijing, China.

0148-0227/11/2010JA016376

do not substantially change relativistic electron fluxes, while the remaining 50% result in a net flux enhancement [*Dessler and Karplus*, 1961; *Baker et al.*, 1994; *Li et al.*, 1997; *Kim and Chan*, 1997; *Reeves et al.*, 1998; *Miyoshi et al.*, 2003].

[5] Energetic electrons in the energy range of 50 keV to 6 MeV at geosynchronous orbit are strongly modulated by the solar wind speed along with the polarity of the interplanetary magnetic field (IMF) [*Li et al.*, 2005]. Long-term relativistic electron measurements show strong seasonal and solar cycle variation [*Li et al.*, 2001]. The electron flux is at its most intense during the declining phase of the solar cycle, and at its weakest near the solar minimum; during the ascending phase of the solar cycle, the electron flux increases in intensity. After analyzing the long-term NOAA satellite observations at low altitude, *Fung et al.* [2006] showed that the quiet time slot region exhibits an oscillatory motion in L that is connected to the solar-cycle variations [*Li et al.*, 2006]. The center of the slot is found to be located at slightly higher (L = 3) during a solar maximum and at lower L (L = 2.5) at solar minimum.

[6] Most of the recent studies have been focusing on the dynamics of fluxes in the heart of the outer radiation belt. However, *Li et al.* [2006] showed that there is a correlation between the inner edge of the outer radiation belt and the innermost location of the plasmapause. They suggested two mechanisms by which the plasmapause may play a role in modifying the acceleration processes: the plasmasphere may modify the characteristics of the ULF waves that diffuse particles radially inward and to higher energies, and acceleration by VLF chorus may produce a flux peak [e.g., *Green and Kivelson*, 2004; *Chen et al.*, 2006; *Iles et al.*, 2006; *Shprits et al.*, 2007] just outside the plasmasphere because chorus is strongest just beyond the plasmapause. Using SAMPEX observations, *Tverskaya et al.* [2003], *Baker et al.* [2004], *Goldstein et al.* [2005], and *O'Brien et al.* [2001] showed a close relationship between the plasmapause location and the inner extent of the outer belt during geomagnetic storms.

[7] *Zheng et al.* [2006] studied the long-term behavior of relativistic electrons in the slot region (L = 2 − 3) and in the inner belt ($L < 2$) by using the daily-averaged 2–6 MeV electron fluxes obtained from the SAMPEX satellite during 1992–2004. They found that the enhancements of the inner belt electron flux occur during the time intervals of high solar wind speed and a large negative *Dst*. The flux enhancement was found to be coincident with low solar wind density and high *Kp* and *AE* values. Their conclusion was that a large negative *Dst* alone is not sufficient to create an inner belt electron flux enhancement, high average solar wind speed is required too.

[8] Measurements of radiation belts have been made on many satellites in the inner magnetosphere, including SAMPEX, Polar, GPS, CRRES, LANL geosynchronous, GOES, and HEO [*Friedel et al.*, 2002]. While we have a lot of data that reveal the complexity of the radiation belts' dynamics, we still do not have enough experimental information to enable a comprehensive study of the relative importance of the various mechanisms for acceleration and loss. Therefore, the data, which do not contain direct measurements of the radiation belts fluxes but rather indirect effects from the presence of energetic particles in the radiation belts, are of a great value too.

[9] In the present paper, we demonstrate how the background counts produced by energetic electrons and ions of the radiation belts in the Cluster CIS and Double Star HIA instruments (see more description on the instruments in the next section) can be interpreted to obtain the locations of the boundaries of the outer and inner belts. During the analyzed period (years 2007–2009), corresponding to the recent solar minimum, Cluster was very close to the Earth with a perigee around L = 2. We identify the boundaries of the outer and inner belts from the ion spectrograms measured by Cluster and Double Star and study their evolution with time and their dependence on solar wind parameters and geomagnetic indices. We also focus on the variations of the outer boundary of the outer belt as it shifts earthward and tailward during that time period and on the changes in slot region thickness. We show that the boundaries determined from the background measurements can be an additional source of useful information for the radiation belts' model development and validation.

2. Cluster Measurements

[10] The Cluster mission consists of four identical spacecraft launched in year 2000 on similar elliptical polar orbits with an initial perigee at about 4 R_E and an apogee at 19.6 R_E [*Escoubet et al.*, 2001]. This allowed Cluster to cross the ring current region, the radiation belts and the outer plasmasphere, from south to north, during every perigee pass, and to obtain their latitudinal profile, following almost the same flux tube [*Vallat et al.*, 2005; *Dandouras et al.*, 2005]. Moreover, because of the annual precession of its orbit, Cluster crosses the equator at all MLT ranges over a year.

2.1. Cluster CIS Instrument

[11] The Cluster Ion Spectrometry (CIS) experiment on board Cluster consists of the two complementary spectrometers, the Composition and Distribution Function Analyzer (CODIF) and the Hot Ion Analyzer (HIA), and provides the three-dimensional ion distribution functions (about 0–40 keV/q) with one spacecraft spin (4 s) time resolution [*Réme et al.*, 2001]. The time-of-flight mass-resolving spectrometer CODIF provides the ion composition of the plasma separately for each of the major magnetospheric species (H+, He++, He+, and O+), from a thermal energy of 0.02 to about 40 keV/q, thus covering a substantial part of the ring current energy range. The HIA sensor measures ions in the energy range of 5 eV/e to 32 keV/e. It does not provide mass discrimination but has a good angular resolution (5.6°). Both CODIF and HIA use an electrostatic analyzer to select incoming ions as a function of their energy. The magnetic field data used come from the FGM (Fluxgate Magnetometer) experiment on board Cluster [*Balogh et al.*, 2001].

2.2. Recent Changes in Cluster Orbits

[12] The CLUSTER orbit is subject to various perturbations: Lunar attraction, oblateness of the shape of the Earth, drag etc. Recently, due to orbit deformations, the perigee of the Cluster orbit shifted closer to the Earth, from about 4 R_E in the year 2000 to about 1.3 R_E in the year 2010, bringing it deep inside the radiation belts' region.

[13] Orbital manoeuvres have also been performed, but these are done to either control the size and geometry of the

tetrahedron or to mitigate the effects of the perturbations (e.g. perigee raise manoeuvres, to avoid early atmospheric re-entry). Due to Sun-Moon orbit perturbations, the apogee of the Cluster spacecraft has been slowly drifting away from Earth to reach an altitude above 130,000 km (above about 21 R_E). To maintain a good communication link with ground stations, the apogees of the four Cluster spacecraft were lowered in November 2009 by about 5,000 km resulting in a reduced orbit period of around 54 hours 35 minutes. In addition, the orbit inclination has drastically changed from its original polar orbit and will have a much lower inclination in the coming years.

3. Double Star HIA Instrument

[14] During 2004–2007 the joint European Space Agency/Chinese Double Star TC-1 spacecraft has provided an additional point of measurement to Cluster measurements and on a larger scale: the Cluster and Double Star orbits are such that the spacecraft are almost in the same meridian, allowing conjugate studies. The equatorial spacecraft (TC-1) was launched into an elliptical orbit of 1.09–13.4 R_E, inclined at 28.5° to the equator. This enabled it to investigate the regions of the inner magnetosphere and even to get below the inner radiation belt. The TC-1 spacecraft reentered the atmosphere on 14 October 2007. The HIA instrument on board the Double Star TC-1 spacecraft is an ion spectrometer nearly identical to the HIA sensor of the CIS instrument on board the four Cluster spacecraft. This instrument has been specially adapted for TC-1. It measures the 3-D distribution functions of the ions between 5 eV/q and 32 keV/q without mass discrimination [*Réme et al.*, 2005]. The Double Star magnetic field data come from the FGM (Fluxgate Magnetometer) experiment on board TC-1 [*Carr et al.*, 2005].

4. Boundaries of the Outer and Inner Radiation Belts as Observed by Cluster CIS Instruments

[15] In the present study, Cluster CIS spectrograms during perigee passes for the period between April 2007 and June 2009 were analyzed. Figure 1 presents an example of energy versus time spectrograms in counts/second measured by (a) HIA and (b) CODIF instruments on June 30, 2008 during 1010–1215 UT. Cluster reached L = 2.6 at its perigee at dusk around 17 MLT. There are clear signatures, better seen in the CODIF spectrogram (Figure 1b), of the ring current population and ion dispersed structures, such as nose and wedge-like structures reported in earlier studies [see, e.g., *Vallat et al.*, 2007; *Dandouras et al.*, 2009]. Starting from 1040 UT, significant background can be clearly noticed, especially in the HIA spectrogram (Figure 1a). Cluster comes so close to the Earth that penetrating particles from the radiation belts can go through the instrument walls and directly hit the detectors. Such penetrating particles induce a background on the instrument's counting. This background appears as a substantial, homogeneous increase of count rate over all energy channels in the energy versus time ion spectrograms.

[16] The spectrograms presented here are in raw counts per second, contrary to the standard plots, where ion counts per second are usually corrected for the detector efficiency. The correction for efficiency is performed assuming that these are ions within the energy range of the detector. The detector energy-dependent efficiency is an increasing function of ion energy. This implies that the low-energy channels (smaller efficiency) have stronger correction, which artificially boosts their apparent count rates. For penetrating high-energy particles, however, this energy-dependent efficiency is not applicable, because these particles have energies much higher than those provided in the instrument calibrations.

[17] The energy in the ordinate scale of a spectrogram is the electrostatic analyzer selected energy for ion detection, which for the HIA sweeps from 32 keV/e down to 5 eV/e. The penetrating particles, however, are not affected by the electrostatic analyzer voltage and can induce a detection signal during any step of the analyzer energy sweep. The homogeneous count rate that appears then in all instrument energy channels confirms that this is indeed a penetrating particle background, which is independent of the instrument energy-sweep cycle. The only energy channel that presents slightly higher counts is the lower channel of HIA (5–8 eV), which is due to plasmaspheric ions being detected together with the background.

[18] For the CODIF instrument, background rejection is much more efficient than for HIA. CODIF is a time-of-flight ion mass spectrometer, using two detection signals to validate ion detection: a "start" signal and a "stop" signal, separated in time by a valid time-of-flight interval corresponding to the ion velocity. This double signal coincidence technique helps in eliminating most of the penetrating particles, which produce only "single" signals. However, in very intense radiation environments, there is a finite probability of two uncorrelated penetrating particles generating two signals (one each), one mimicking a "start" signal and the other mimicking a "stop" signal, and being separated by a "valid" time-of-flight interval. In these cases some background is induced in the CODIF data.

[19] The appearance and disappearance of the background counts in all energy channels mark the entry to and leave from the outer and inner radiation belts. Therefore, it is possible to locate the boundaries of the outer and inner radiation belts. In Figure 1 they are marked by vertical black lines. Six boundaries can be identified and we define them as following: B1, outer boundary of the outer radiation belt (first crossing when Cluster enters the outer belt moving inbound from higher L-shells); B2, inner boundary of the outer radiation belt (first crossing when Cluster leaves the outer belt moving to lower L-shells); B3, outer boundary of the inner radiation belt (first crossing when Cluster enters the inner belt close to its perigee); B4, outer boundary of the inner radiation belt (second crossing when Cluster leaves the inner belt close to its perigee); B5, inner boundary of the outer radiation belt (second crossing when Cluster enters the outer belt moving outbound to higher L-shells); B6, outer boundary of the outer radiation belt (second crossing when Cluster leaves the outer belt moving from lower L-shells).

[20] We define the boundary as a location, where the sharp increase of counts is seen simultaneously in all energy channels. Additional indicator of the inner belt boundaries comes from the strong background which CODIF gets in the harsh environment of the inner belt, albeit the time-of-flight technique.

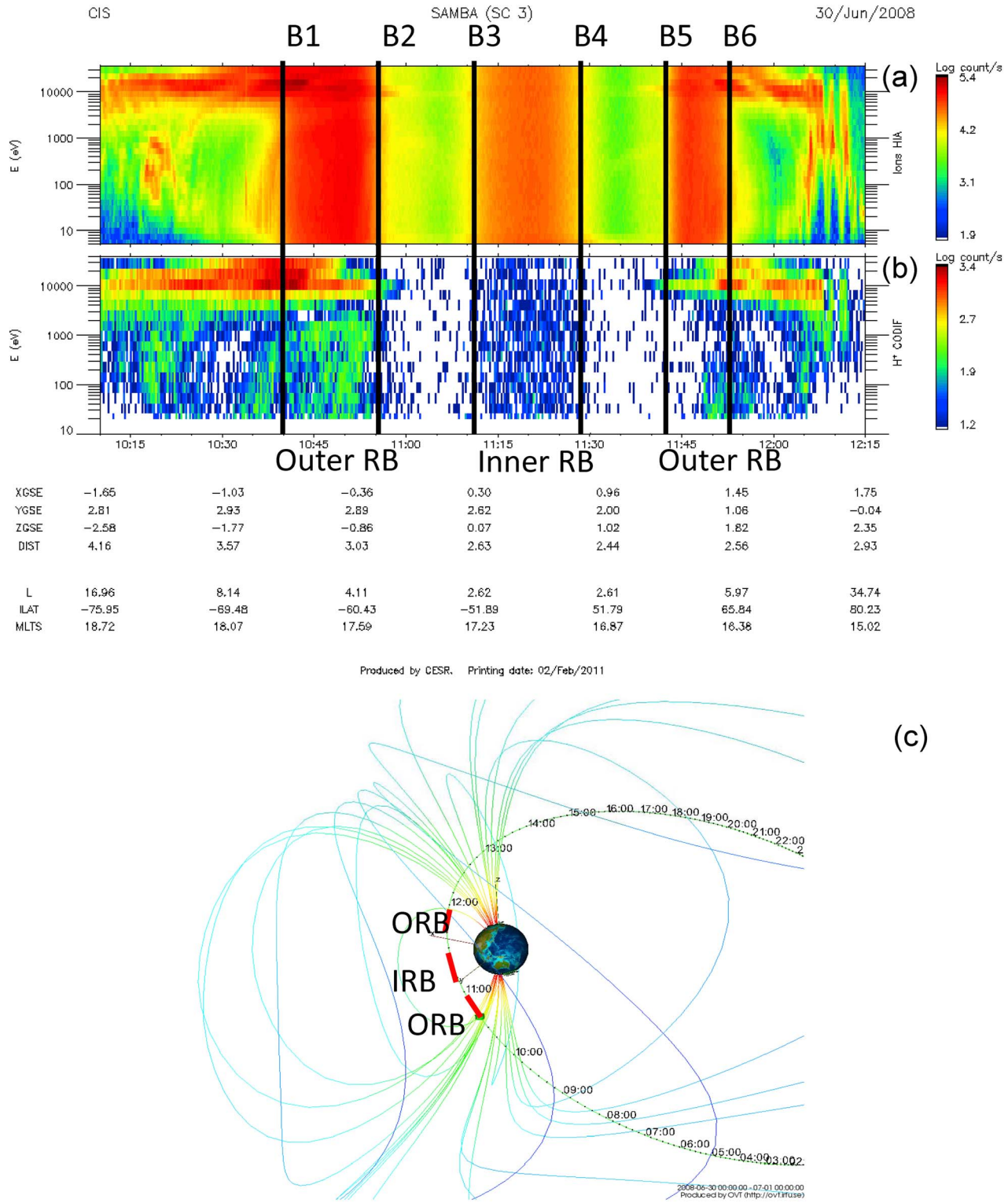

Figure 1. Example of energy versus time ion spectrograms in counts/second measured by the (a) HIA and (b) CODIF instruments on June 30, 2008 during 1010–1215 UT. Locations of radiation belt boundaries identified from the detected background are marked by black vertical lines. (c) Cluster SC3 orbit is shown projected on *Tsyganenko* [1989] T89 magnetic field model with segments when spacecraft were in the radiations belts marked red. Orbit Visualization Tool (OVT) plot courtesy of the OVT team.

[21] To determine a boundary location, a rather simple algorithm was used. The background appears as a substantial, homogeneous increase of count rate over all energy channels in the energy versus time ion spectrograms. The appearance of such a substantial background indicates, at a first instance, the spacecraft entry into a radiation belt. We define the boundary visually as a location, where the sharp increase of counts is seen simultaneously and the background is the same in all energy channels. To define the boundary position more accurately, we then follow the evolution of counts/sec with time for all 31 energy channels and analyze the changes $\frac{\Delta c/s}{\Delta t}$, step by step in time. We then determine the first time moment, when the $\frac{\Delta c/s}{\Delta t}$ are the largest and same for all energy channels (sharpest gradient) and place a boundary there. In this process we compare two time steps before and two time steps after of each time moment.

[22] As can be noticed on HIA spectrogram, when we try to determine the outer boundary of the outer belt, in addition to the background, we can also see some populations measured with energies above 5 keV and below 1 keV. They are real ring current populations and ion dispersed structures [*Vallat et al.*, 2007; *Dandouras et al.*, 2009], which can also be proved by the existence of similar structures in the CODIF spectrogram at the same time. Thus, the formal method described above for identifying the boundaries can be, in these cases, inaccurate in some energy channels. To avoid significant errors in determination of boundaries, all the locations of boundaries were checked visually for all spectrograms. When such ion populations were present, the corresponding energy channels were excluded from for the $\frac{\Delta c/s}{\Delta t}$ calculation for the determination of the outer boundary of the outer belt. This allows removing the effects from the real ring current ion populations in the background determination.

[23] Figure 1c presents the Cluster SC3 orbit for the June 30, 2008 perigee pass, projected on the *Tsyganenko* [1989] T89 magnetic field model. We present this plot to illustrate the location of a satellite in the magnetosphere. The segments of the orbit during which the spacecraft were in the radiation belts, as determined from the CIS instrument background, are marked with red curves. Cluster was in the outer radiation belt (ORB) during 1040–1055 UT, in the inner belt (IRB) during 1110–1130 UT and again in the outer radiation belt (ORB) during 1140–1155 UT. The Orbit Visualization Tool (OVT) plot is courtesy of the OVT team.

[24] Similarly to Figure 1, Figure 2 shows two other typical energy versus time spectrograms observed by Cluster CIS instruments on (a) August 21, 2007 during 1020–1210 UT and on (b) January 30, 2009 during 1600–1745 UT. During the year of 2007 (Figure 2a), the Cluster perigee was at around L = 3, which is above the inner radiation belt. Therefore, only the outer (B1 and B6) and inner (B2 and B5) boundaries of the outer radiation belt can be identified. Figure 2b corresponds to the year 2009, when Cluster came as close to the Earth as L = 2, and the two outer boundaries (B3 and B4) of the inner radiation belt can be detected. The background counts in the regions of the outer radiation belt are rather weak so the boundaries of the outer belts are not distinct. This may be either due to the orbit location, when satellite passes at higher magnetic latitudes and measures higher pitch angles or because the outer radiation belt is so weak that no background comes from it. All three types of spectrograms (Figures 1 and 2) were analyzed and the locations of boundaries were determined. Depending on satellite orbit and time, when the boundaries were identified, four, six or only two boundaries can be determined.

[25] In the present study we use only the background information to locate the boundaries of the radiation belts but we have neither any direct ways to estimate the energies of the radiation belts particles producing this background nor fluxes of these particle. It is possible, however, to estimate the lowest energy of particles penetrating into the instrument detector from the thickness of the aluminum (Al) shielding used in the instrument. Figure 3 shows the dependence of energy in MeV of penetrating particles on the thickness of Al shielding. The upper curve represents protons and the lower curve electrons. For HIA and CODIF at Cluster (marked with red), the shielding is about 4–7 mm thick depending on particle arrival direction.

[26] For electrons, we can assume that the measured background comes from the particles, which have energies above 2 MeV. For both outer (with electrons as main constituents) and inner (with significant proton flux) radiation belts the locations of the boundaries that we detect contain the locations of boundaries from electron contamination with energies above 2 MeV. To prove this, several simple runs of the Casino (Monte Carlo Simulation of Electron Trajectory In Solids) simulation software (http://www.gel.usherbrooke.ca/casino/index.html [*Drouin et al.*, 2007]) were made (not shown here). This program is a Monte Carlo simulation of electron trajectory in solid specially designed for low beam interaction in a bulk and thin foil. Electrons with energies of 1, 2 and 4 MeV were considered. It was obtained that all 1 MeV electrons (and most of 2 MeV electrons) are stopped before they penetrate 2 mm depth of Al. All 2 MeV electrons are stopped before they penetrate 4 mm depth of Al. This confirms the estimate of penetration of energetic electrons with energies above 2 MeV.

[27] The inner radiation belt is dominated by protons ("proton belt") with energies of tens of MeVs. Energetic proton fluxes can significantly exceed those of electrons, and the background coming from MeV protons can not be negligible compared to the electron background [see, e.g., *MacDonald et al.*, 2006]. The inner belt boundaries B3 and B4 mark the appearance of the background from both electrons and protons. Using Figure 3 we determine the low threshold energy for the proton background as 30 MeV. Similarly as for electrons, to prove this energy threshold estimate, the SRIM (The Stopping and Range of Ions in Matter) simulation software (http://www.srim.org/[*Ziegler et al.*, 2010]) was used to calculate the stopping and range of the protons of energies 10, 20, 30, and 50 MeV into matter using a quantum mechanical treatment of ion-atom collisions. It was obtained (not shown here) that all 10 MeV protons are stopped before they penetrate even in 1 mm depth of Al, and all 20 MeV protons are stopped at around 2 mm depth of Al. This shows that protons with energies below 20 MeV cannot reach the detector, because nowhere the instrument walls are less than 2 mm total thickness. 30 MeV protons, however, can traverse the 4 mm typical total thickness of Al, contributing to the background, which agrees with our estimates from Figure 3.

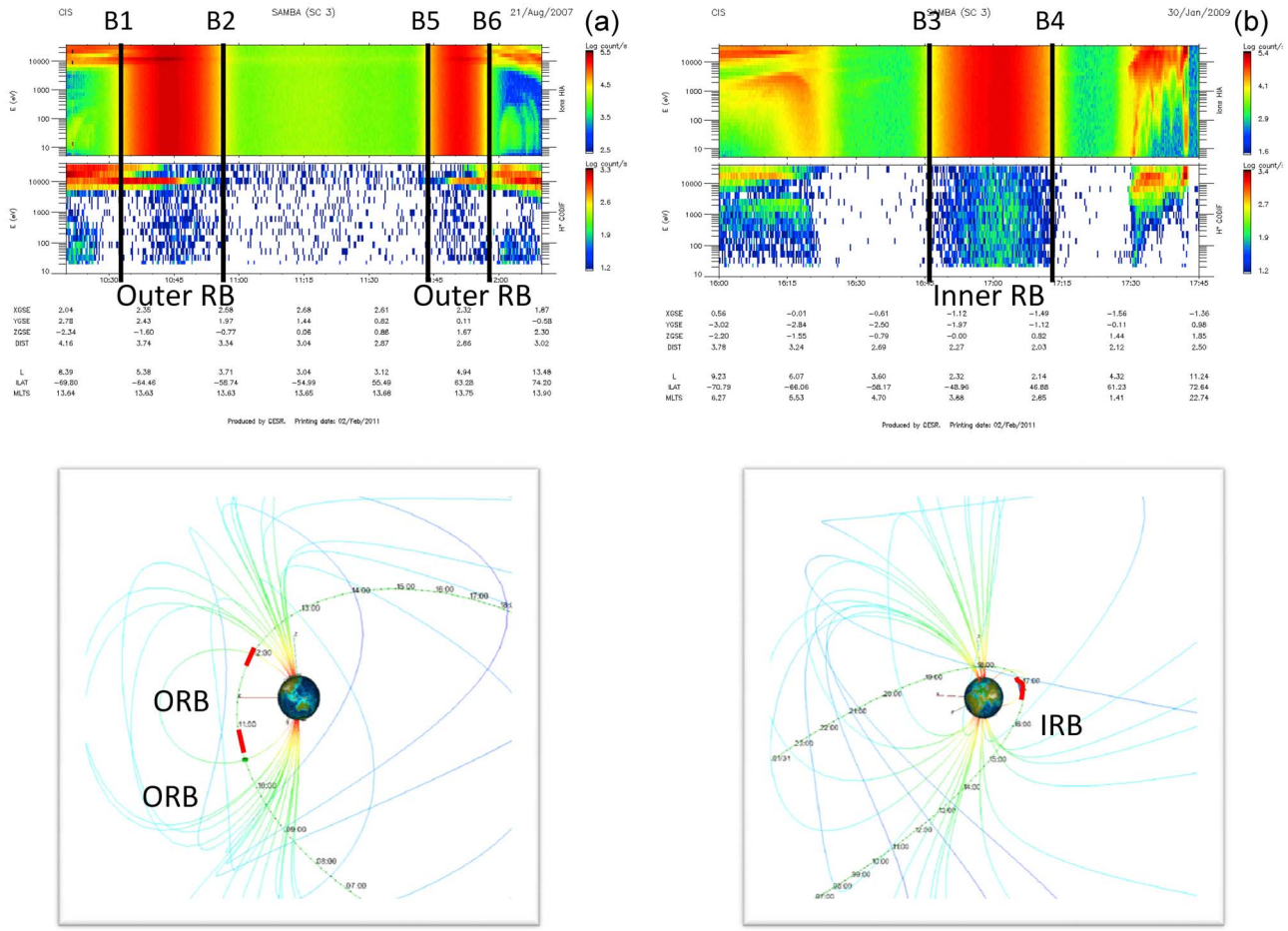

Figure 2. Two other typical energy-time spectrograms observed by Cluster CIS instruments on (a) August 21, 2007 and on (b) January 30, 2009 together with Cluster SC3 orbits projected on *Tsyganenko* [1989] magnetic field model.

[28] In addition to energetic electrons and protons of the radiation belts, the contamination can also come from the gamma-rays emitted by incoming electrons via Bremsstrahlung process [see, e.g., *Kasahara et al.*, 2009]. Gamma radiation can also be produced when energetic electrons bombard materials and the excited atoms within emit characteristic "secondary" gamma rays. This process is efficient for >1 MeV electrons but gamma rays from 100 keV elec-

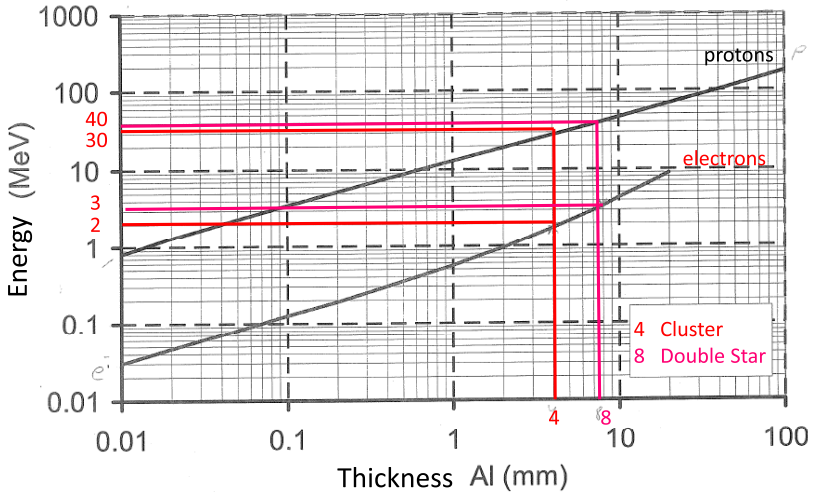

Figure 3. Dependence of the energy in MeV of penetrating particles on the thickness of Al shielding (courtesy of D. Boscher).

trons can also cause significant background. The fluxes of lower-energy 100 keV electron in the radiation belts are high (10^3–10^4/cm^2 s sr keV), which is much higher than the flux of "directly detected" MeV electrons. Therefore, the analyzed background on Cluster CIS spectrograms can possibly contain the effects from MeV and lower-energy (down to 100 keV) electrons. In addition, the generation of gamma-rays by the sub-MeV electrons (i.e., above 300 keV) can also add to the contamination in the radiation belts.

[29] We used the Casino simulation software to study the effect from the secondary gamma-rays in more details. Our simulations (not shown here) demonstrated that, indeed, the bremsstrahlung-produced gamma-rays produced from the energetic electrons with energies around and above 100 keV can penetrate the detector. Once gamma-ray photons get into the detector, their signal is indistinguishable from that of the parent energetic electrons.

[30] In order to assess this background from gamma-rays, we examined the instrument response in the presence of 100 keV electrons. This was done for a strong substorm event (10 August 2004, AE = 800 nT), when we analyzed the data acquired in the plasma sheet by IES energetic electron (37 to 400 keV) instrument of the RAPID experiment [*Wilken et al.*, 1997] and CIS (HIA and CODIF) energy-time spectrograms onboard Cluster. IES instrument detected substantial electron fluxes with energies around 100–200 keV (of the order of a few 10/cm^2 s sr keV) but no background was detected by CIS instrument, which it would have certainly detected, if it were sensitive to 100 keV electrons. Selecting a plasma sheet event for such an analysis presents the advantage of being completely outside the radiation belts, and thus outside of the MeV populations.

[31] For the analyzed event, the background from gamma-rays was undetectable, and we can assume that gamma-ray contamination is negligible as long as 100 keV electron fluxes are not very high. However, gamma-rays from intense fluxes of a few hundred keV electrons can eventually contribute to instrument background. Thus, the 2 MeV threshold for penetrating electrons is not an absolute one.

[32] We must keep in mind that the background comes from the energetic electrons, protons and also secondary gamma-rays, when we try to determine from this background the boundaries of the radiation belts and discuss their locations.

[33] The 4–7 mm Al thickness is accumulated, total thickness along straight lines. Individual elements are thinner, and some scattering of penetrating particles between them cannot be excluded. There can be also some paths where the total thickness is less than 4 mm, but these represent extremely narrow solid angles, and their contribution to the total penetrating flux should be negligible. We note also that nowhere the instrument is less than 2 mm of total Al thickness.

5. Boundaries of the Outer and Inner Radiation Belts as Observed by Double Star

[34] We also analyzed the HIA spectrograms on perigee passes from the Double Star TC-1 satellite during the period of May 15, 2007 to September 28, 2007. Figure 4 presents the Double Star HIA spectrogram in raw counts/second measured on August 8, 2007 during 1700–2000 UT (Figure 4a), the L-value of the satellite's orbit (Figure 4b), and the Double Star TC-1 orbit projected on *Tsyganenko* [1989] T89 magnetic field model (Figure 4c). The white gap seen on the spectrogram is a data gap due to an eclipse as the spacecraft goes behind the Earth. At perigee, Double Star is at very low altitudes (L = 1.15), so it detects the ionosphere/lower plasmasphere.

[35] The background measured by the Double Star HIA instrument is rather similar to that of the Cluster HIA, with the difference being that on Double Star the Al shielding is 4 mm thicker. Additional shielding moves the penetrating particle threshold to higher energies. Electrons with energies above 3 MeV and protons with energies above 40 MeV penetrate the detector (Figure 3). We also can not rule out the background coming from gamma-rays produced by lower-energy electrons of about 100 keV or more. Similar discussion, which was presented for CIS background measurements is valid here. Analyzing the spectrograms, we can identify five boundaries such as B2, inner boundary of the outer radiation belt (first crossing when Double Star leaves the outer belt moving inbound to lower L-shells); B3, outer boundary of the inner radiation belt (first crossing when Double Star enters the inner belt inbound, close to its perigee); B0, inner boundary of the inner radiation belt (Double Star leaves the inner belt and starts to detect the ionosphere/lower plasmasphere at even lower L-shells, at few eV); B4, outer boundary of the inner radiation belt (second crossing when Double Star leaves the inner belt outbound, close to its perigee); B5, inner boundary of the outer radiation belt (second crossing when Double Star enters the outer belt moving to higher L-shells).

[36] HIA instrument onboard Double Star has the better shielding that results in a lower background in the outer radiation belt. As can be seen in Figure 4, the background at the outer boundaries of the outer radiation belt is weak and gradual, without clear, sharp increase. Boundaries B1 and B6 of the outer radiation belt were not identified on the Double Star HIA spectrograms due to high ambiguity of a boundary location.

[37] Four of the boundaries (B2, B3 and B4, B5) are seen on Cluster too, but B0 is seen only on Double Star. We applied the same method of identification of boundaries. We define the boundary as a location, where the sharp increase of counts is seen simultaneously in all energy channels.

6. Cluster CIS Measurements

6.1. L-MLT Locations of Radiation Belts Boundaries

[38] The boundaries of the outer and/or inner radiation belts were identified on 241 Cluster CIS spectrograms on perigee passes. The actual number of boundaries is larger since, as shown above, on one spectrogram most of the times several boundaries can be detected. Figure 5a shows the L-MLT locations of all identified boundaries during the period between April 2007 and June 2009. Outer boundaries of the outer radiation belt are B1 (blue diamonds) and B6 (light blue open diamonds), inner boundaries of the outer radiation belt are B2 (green circles) and B5 (orange open circles), and outer boundaries of the inner radiation belt are B3 (red stars) and B4 (magenta open stars).

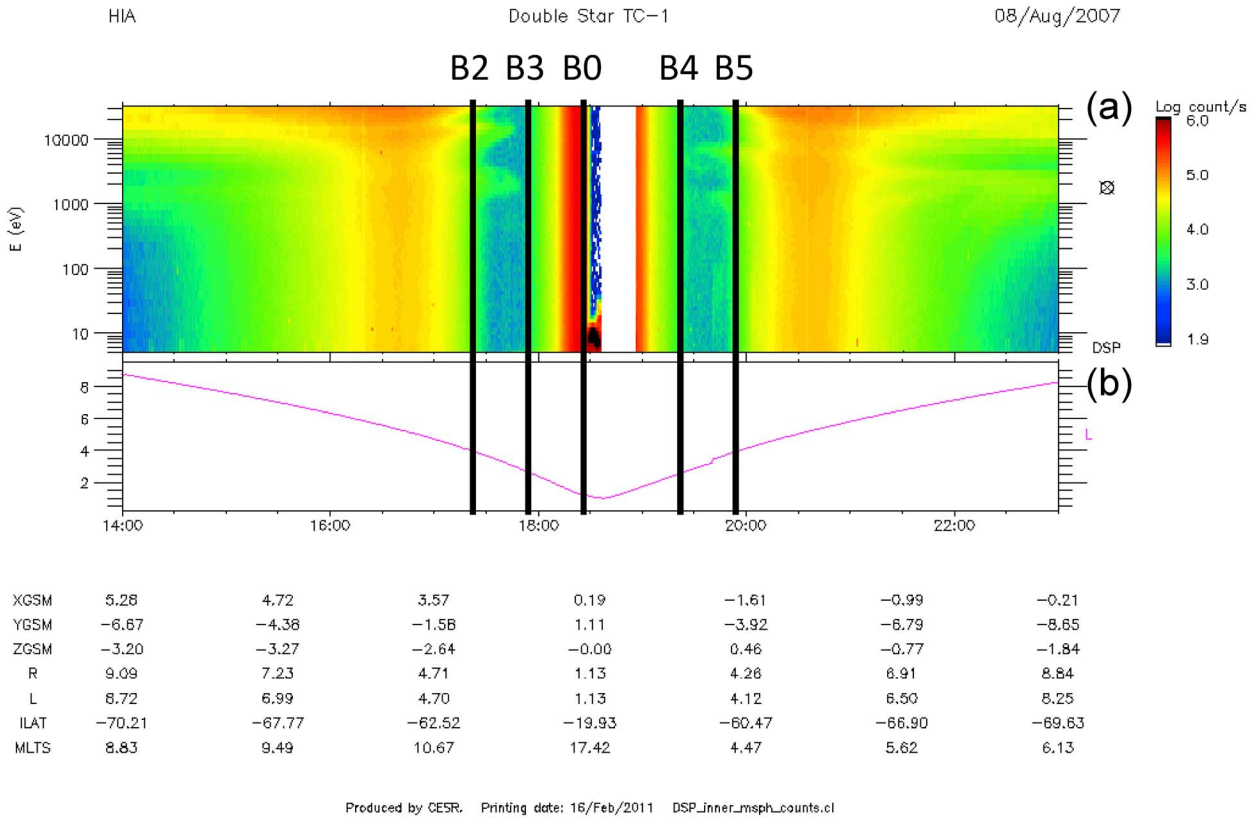

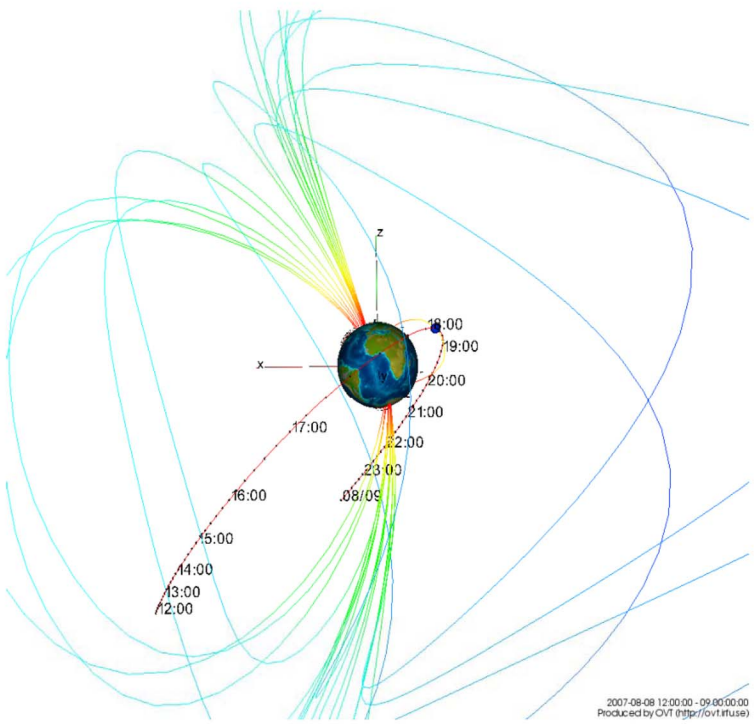

Figure 4. (a) Double Star HIA spectrogram in counts/second measured on August 8, 2007 during 1700–2000 UT, (b) L-value of the satellite's orbit, and (c) Double Star TC1 orbit projected on *Tsyganenko* [1989] T89 magnetic field model. The white gap seen on the spectrogram is due to eclipse, because the spacecraft is going behind the Earth.

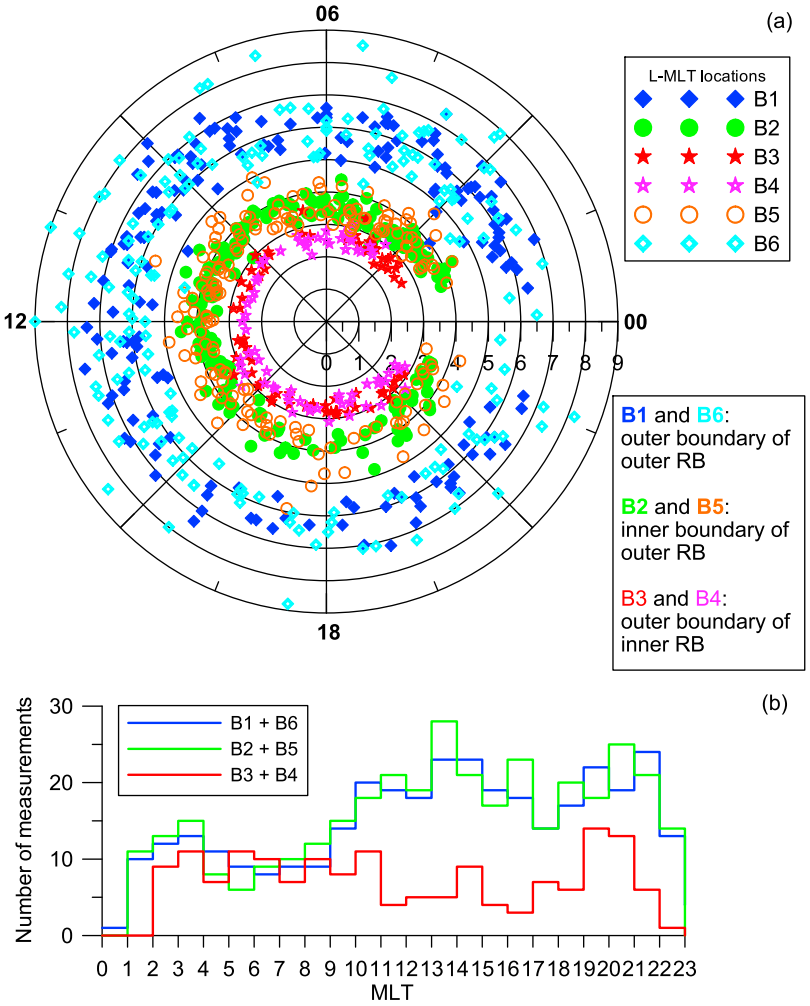

Figure 5. (a) L-MLT locations of all identified boundaries during the period between April 2007 and June 2009 (Cluster CIS data). Outer boundaries of the outer belt are B1 (blue diamonds) and B6 (light blue open diamonds), inner boundaries of the outer belt are B2 (green circles) and B5 (orange open circles), and outer boundaries of the inner belt are B3 (red stars) and B4 (magenta open stars); (b) number of detected boundaries per one hour of MLT as the total numbers for B1 and B6 (blue step-like line), B2 and B5 (green step-like line), and B3 and B4 (red step-like line) boundaries.

[39] Figure 5b presents the number of the determined boundaries per 1 hour of MLT, showing the total numbers for B1 and B6 (blue step-like line), B2 and B5 (green step-like line), and B3 and B4 (red step-like line) boundaries. There were two times more observations, when Cluster was on the dusk side than on the dawn side for the boundaries of the outer belt. The number of the observed inner belt boundaries was similar to the outer belt boundaries at dawn and dropped during noon-afternoon hours. There were very few observations around midnight, due to solar eclipses, when the spacecraft gets behind the Earth, and the instrument is switched off.

[40] The Maglib library (http://logiciels.cnes.fr/MAGLIB/en/logiciel.htm) was used to calculate the corresponding L-values with IGRF 2000 model for the internal magnetic field and Tsyganenko T89 for the external field. As always when using models, the ambiguity of mapping point due to the inaccuracy of the model exists. Since the analyzed time period was very quiet, the average configuration of the magnetospheric magnetic field given by Kp-dependent T89 model was assumed to be reasonable enough. Other non-storm time models will not give results which are critically different from T89 model (M. Kubyshkina, private communication, 2010).

[41] The obtained distribution of boundaries reflects the general structure of the radiation belts. The inner belt is rather stable, with no large variations of the locations of B3 and B4 boundaries. All B3 and B4 boundaries are inside L = 2.5–3. The inner boundaries of the outer belt (B2 and B5) exhibit more variability covering the range of L between 3 and 5. The outer boundary of the outer belt is the most variable. The corresponding boundaries B1 and B6 were detected on the wider L interval from 4.5 to 9. The MLT coverage depends on the Cluster orbit (see Figures 1 and 2).

[42] B1 and B6 are thus the most variable boundaries, and we do not expect them to coincide. Their differences are not due to the inaccuracy of the magnetic field model. They are

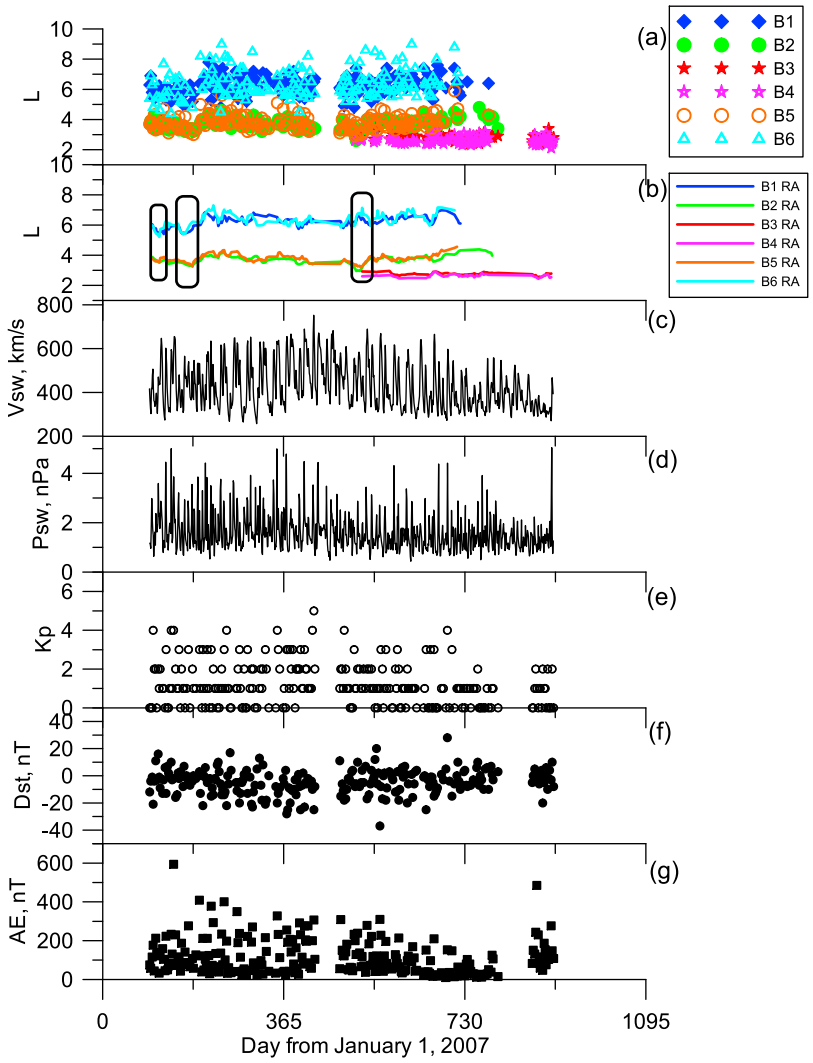

Figure 6. (a) Time-dependent locations of the radiation belts boundaries in L shown with the same color symbols as in Figure 5 and (b) as running averages instead of symbols with the same color. Daily averages of the (c) solar wind speed and (d) solar wind dynamic pressure are shown in Figures 6f and 6g. Shown are geomagnetic indices, such as (e) *Kp* (open circles), (f) *Dst* (black circles), and (g) *AE* (black squares), taken and averaged at times when boundaries were identified at 241 Cluster CIS spectrograms. Three time intervals, marked by black ovals, are to be studied in more details.

not determined at the same time moments and they are at different parts of the satellite orbit.

6.2. L Versus Time Locations of Radiation Belts Boundaries

[43] Figure 6 presents time-dependent locations of the boundaries in L shown with the same color symbols (Figure 6a) as in Figure 5 and as running averages instead of symbols with the same color (Figure 6b). Running averages were made as spline smoothing with spline tension factor of 2. As was shown in Figures 1 and 2, depending on satellite orbit and time, when the boundaries were identified, four, six or only two boundaries can be determined.

[44] Daily averages of the solar wind speed (Figure 6c) and solar wind dynamic pressure (Figure 6d) are shown in Figures 6f and 6g. The three bottom panels present geomagnetic indices, such as *Kp* (open circles) (Figure 6e), *Dst* (black circles) (Figure 6f), and *AE* (black squares) (Figure 6g), taken and averaged at times when boundaries were identified in the 241 Cluster CIS spectrograms. As can be noticed in Figure 6, during the period between April 2007 and June 2009, when radiation belts boundaries were determined: (1) solar wind speed V_{sw} shows the presence of high speed streams (HSS) with a decrease of their magnitude and appearance starting in the year 2009; (2) solar wind dynamic pressure P_{sw} is quite low, with an average value around 2 nPa with some spikes reaching 5 nPa, which disappear during the year 2009; (3) average *Kp* stayed below 3, with its largest values reaching 4 (5 only once) and showing a decrease from 2 to 1 starting in March 2008 that continued until the beginning of 2009, after that, conditions became even more quiet; (4) no big storms happened, *Dst* varied within about (+20; −20 nT), no significant trends in *Dst* variation were observed; (5) average *AE* was no more than

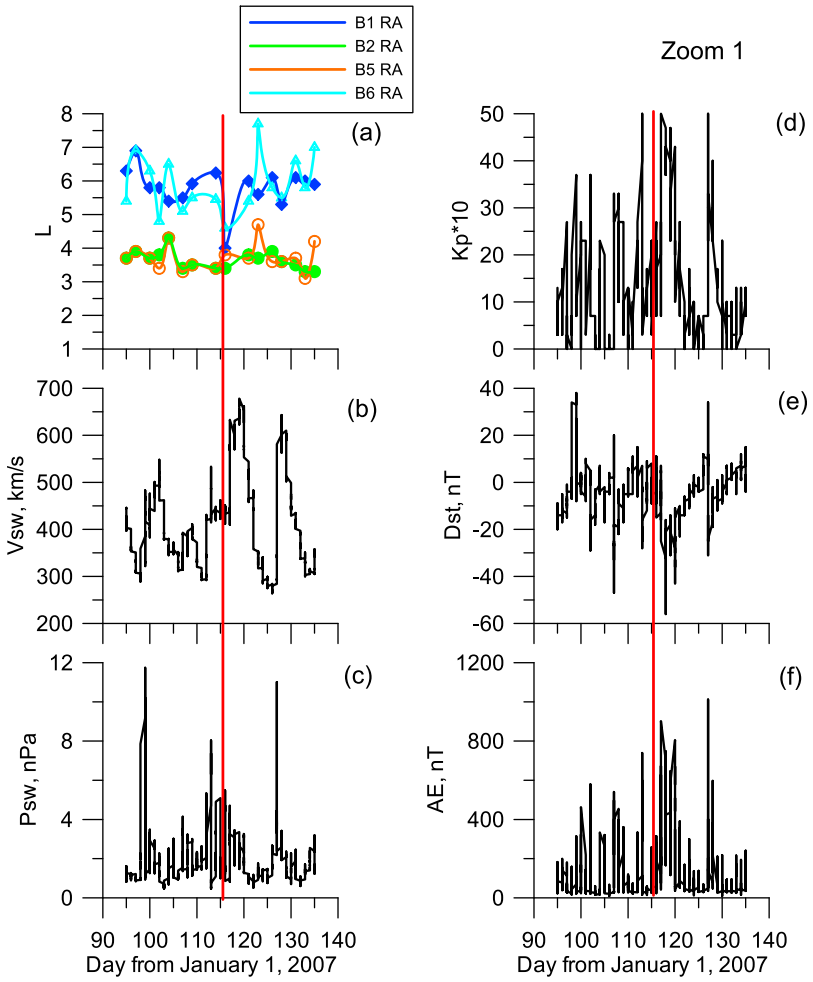

Figure 7. April 5, 2007 to May 15, 2007 period for detailed analysis: (a) L-locations the outer and inner boundaries of the outer belt by symbols and running average curves, corresponding (b) solar wind speed, (c) solar wind dynamic pressure, (d) *Kp*, (e) *Dst*, and (f) *AE* indices. Vertical red lines mark the time moment, when B1 boundary was closest to the Earth.

200 nT, with the max reaching 400 nT, except for just 2 events with 500 and 600 nT, and decreased from March 2008 until the beginning of 2009, with a small increase in the middle of 2009.

[45] Since the variations in solar wind data and geomagnetic indices were rather small, no significant long-term correlations between them and the determined locations of radiation belts boundaries can be found. At the same time, looking at the L-locations of the boundaries as running averages (Figure 6b), several dips to lower L-shells can be seen in the outer boundaries of the outer belt, which is the most variable boundary because it responds to the changes in the solar wind and geomagnetic activity. These dips to low L-shells mark dropouts of outer radiation belt. We select three time intervals, which contain dips to low L-shells, as examples to study in more detail, and they are marked by black ovals in Figure 6b.

6.2.1. Detailed Analysis of the Outer Belt Outer Boundary Variations

[46] Figure 7 zooms into the first period, between April 5, 2007 and May 15, 2007, selected as an example for detailed analysis, when the outer boundary of outer belt comes to Earth as close as L = 4. Figure 7a shows the L-locations of the outer and inner boundaries of the outer belt by symbols and running average curves (as in Figure 6b). We analyze the B1 boundary, which shifts to L = 4 from L = 5.5 and returns to L = 6. It is necessary to keep in mind that the time interval between measurements in Figure 7a is on the scale of a day (Cluster orbital period). When analyzing dips in the boundary profiles, no conclusions based on shorter-time variations of radiation belts can be made. Together with boundary locations, the corresponding solar wind speed (Figure 7b), solar wind dynamic pressure (Figure 7c), *Kp* (Figure 7d), *Dst* (Figure 7e), and *AE* (Figure 7f) indices are given. Vertical red lines mark the time, when the B1 boundary was closest to the Earth at L = 4.

[47] Before the B1 boundary came to L = 4, there was an increase in V_{sw} from 430 to 540 km/sec, an increase in *Kp* to 5, a short drop in *Dst* to −28 nT, and there was also substorm activity with *AE* reaching 700 nT. P_{sw} exhibited 2 peaks of 8 and 5 nPa. Since the time interval between measurements is on the scale of a day, the exact UTs do not matter much for this analysis.

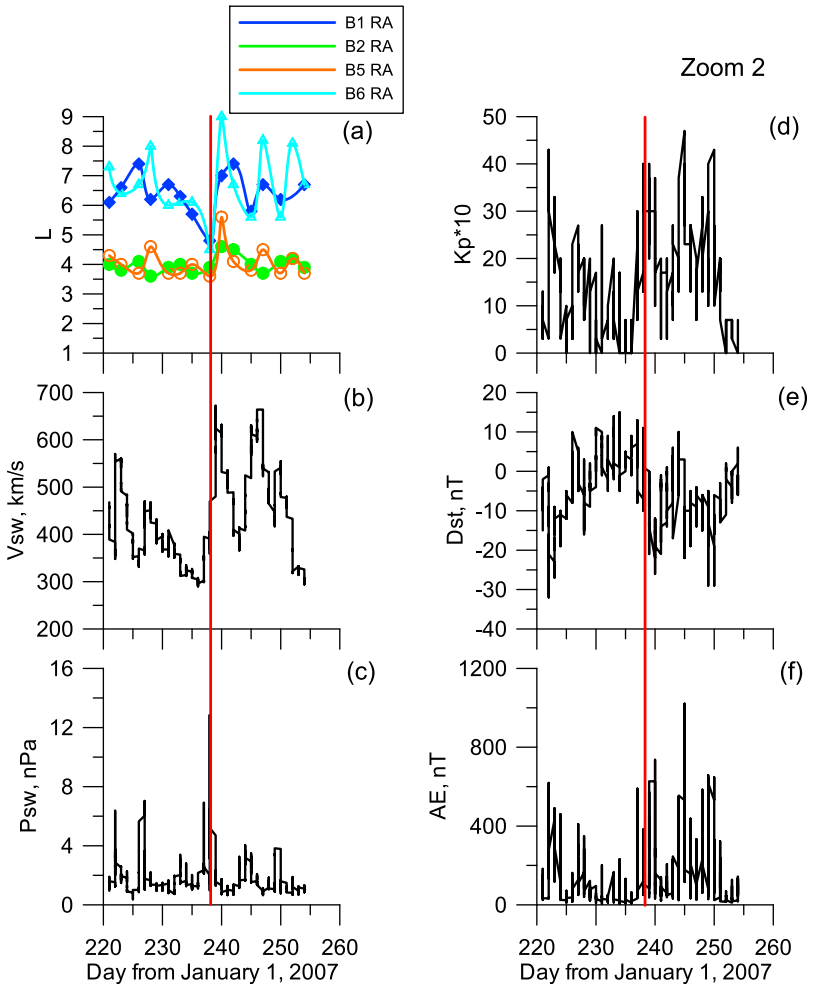

Figure 8. Similar to Figure 7 but for August 9, 2007 to September 11, 2007 period for detailed analysis.

[48] After the dip, when the B1 boundary moves tailward to L = 6, V_{sw} showed a jump from 430 to 650 km/s, *Kp* came to 5 after dropping to 2 during the boundary dip. There was rather small storm-like development in the *Dst* index with a minimum of −50 nT, and obvious substorm activity with *AE* index reaching 800 nT. P_{sw} was low, about 3 nPa.

[49] Figures 8 and 9 show two other example time periods analyzed in detail, one from August 9, 2007 to September 11, 2007 and the other from April 24, 2008 to June 23, 2008. In Figure 8, the B1 boundary came to L = 4.5 from about L = 6 and returned to L = 7. For the third case (Figure 9), the B1 boundary reached L = 4.8 for two earthward shifts from L = 6.5 and 6 and moved back to L = 5.8 and 6.7, respectively. Common features in the solar wind data and evolution of geomagnetic indices are the followings (timescale is day): (1) decrease in the solar wind velocity while the L-value of B1 boundary decreases; (2) increase of the solar wind velocity to 650–700 km/s, indicating the presence of a HSS, right after the boundary's dip; (3) narrow peaks of 6–8 nPa in solar wind dynamic pressure right before the boundary's dip; (4) increased *Kp* (up to 4–5) and *AE* (600–800 nT) right after the boundary dip; (5) *Dst* drops to negative values, around −30 nT, right after the boundary dip.

6.2.2. Focus on the Slot Region

[50] Since the inner boundaries of the outer belt (B2 and B5) and outer boundaries of the inner belt (B3 and B4) were determined, it is possible to study the location and thickness of the slot region situated between them. When the radiation belt slot region is studied it is always assumed that slot between electron outer and inner radiation belts is considered. In our present analysis the slot region defined as a region between the disappearance of the measured background inside the outer belt and the appearance of the background when entering the inner belt, so the measured background contains the contributions from the energetic protons in the inner belt. Figure 10a presents the L locations of part of the identified boundaries during the period between May 23, 2008 and March 7, 2009, which form the slot region. Figure 10b shows the evolution of the slot thickness ΔL, computed as $\Delta L = L_{B2} - L_{B3}$ (open black triangles) and $\Delta L = L_{B4} - L_{B5}$ (black triangles), where L_{Bi} is the L location of the boundary Bi with i = 2,3,4,5. Figures 10c–10g show the solar wind velocity, solar wind

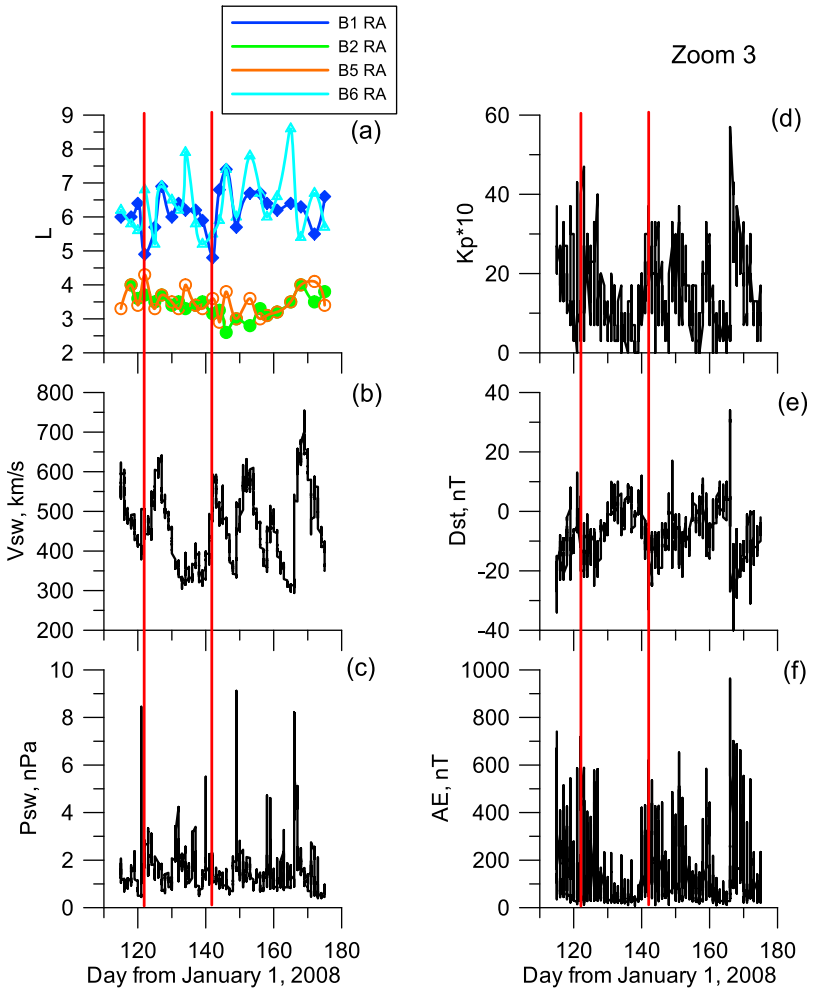

Figure 9. Similar to Figure 7 but for April 24, 2008 to June 23, 2008 period for detailed analysis.

dynamic pressure, *Kp*, *Dst*, and *AE* indices for this period, respectively.

[51] The slot width shows a steady increase from 1–1.5 R_E in November 2008 to 2.5–3 R_E on January 2009. During this period V_{sw} decreases, *Kp* index shows small decrease, while decrease in the *AE* index is more evident. At the same time, *Dst* does not exhibit large variations and P_{sw} shows no significant changes.

7. Double Star Measurements

[52] The boundaries of outer and/or inner radiation belts were identified on 34 Double Star HIA spectrograms on perigee passes. Similar to Cluster CIS spectrograms, the actual number of boundaries is larger since on one spectrogram several boundaries can be detected. Figure 11a shows the L locations of all boundaries identified during the period between May 15, 2007 to September 28, 2007, before Double Star entered the atmosphere. Outer boundaries of the inner belt B3 (red stars) and B4 (magenta open stars), detected at Double Star, are similar to those detected by Cluster, and they are shown with the same colors and symbols as in Figure 5. The inner boundary of the inner belt B0, detected only by Double Star, is shown with black diamonds. Inner boundaries of the outer belt B2 and B5 are the only two similar boundaries, which were identified on Cluster CIS during the same time period as they were on Double Star. Cluster boundaries are plotted in Figure 11a similarly as in Figure 5, as green circles (B2) and orange open circles (B5). To distinguish the similar boundaries detected by the Double Star, boundaries inferred from Cluster measurements are shown as open green circles (B2) and orange circles (B5).

[53] 43(42) of B2(B5) boundaries were identified at CLUSTER and 22(17) on Double Star, respectively. Not every boundary observed at Double Star at a certain date and time had a corresponding boundary observed at CLUSTER at the same date and time. B2 and B5 boundaries observed on CLUSTER and Double Star separately and with running average fit well between the two spacecraft (Figures 11b and 11c). The locations of B2 boundaries vary from L = 3.2 to L = 4.2 when detected on Double Star, and from L = 2.6 to L = 4.8 when identified at Cluster. The mean values are L = 3.6 for Double Star and L = 3.7 for Cluster. For B5 boundaries their locations vary more, they change from L = 3.1 to L = 4.2 for Double Star and from L = 2.9 to L = 5.9

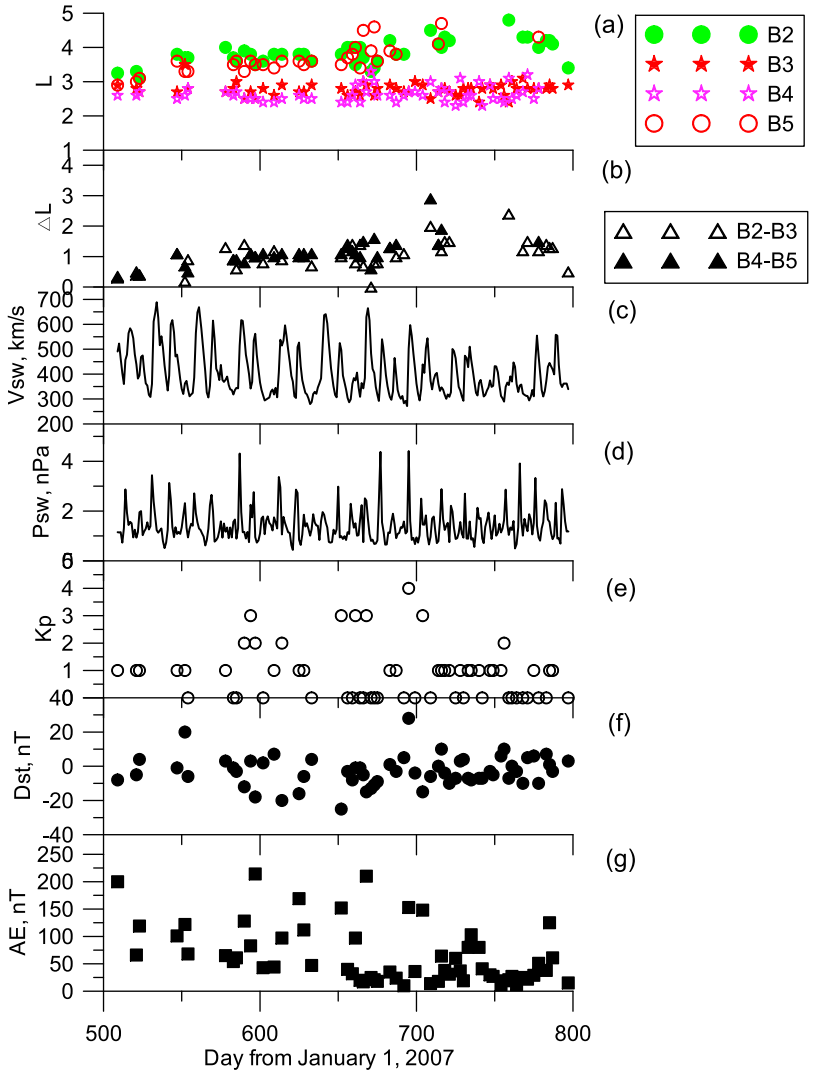

Figure 10. (a) L locations of the boundaries, which form the slot region, (b) the evolution of the slot thickness ΔL, computed as $\Delta L = L_{B2} - L_{B3}$ (open black triangles) and $\Delta L = L_{B4} - L_{B5}$ (black triangles), (c) the solar wind velocity, (d) solar wind dynamic pressure, (e) *Kp*, (f) *Dst*, and (g) *AE* indices for this period.

for Cluster with mean values of L = 3.7 and L = 3.8, respectively. Mean values are quite close to each other. The curves of running averages in Figure 11b go more close than those in Figure 11c.

[54] The boundaries from Cluster and Double star are not expected to be exactly coincident, and one of the reasons for that can be the different energy threshold of the instruments. We show them together on the same plot to demonstrate that these boundaries are located at reasonable L-shells, when measured both on Cluster and Double Star. This proves that the method of determining the boundaries is reliable, when we find similar results using different satellites with similar instruments but still with different threshold.

[55] The boundaries of the inner belt measured by Double Star are stable, with no large variations. The B3 and B4 boundaries are inside L = 2–3. The B0 boundary does not vary much at all, and is located between L = 1.2 and L = 1.3.

[56] Figure 11b shows the evolution of the slot thickness ΔL, computed similarly to Figure 10b as $\Delta L = L_{B2} - L_{B3}$ (open black triangles) and $\Delta L = L_{B4} - L_{B5}$ (black triangles). In contrast to Figure 10b, no trend in the slot thickness can be identified, since the data are too sparse and the time period is too short.

8. Discussion and Conclusions

[57] Cluster CIS spectrograms measured during the period between April 2007 and June 2009, when Cluster was deep in the radiation belts with its perigee as close as L = 2, were analyzed. This time period was during the recent solar minimum, so, in the long-term, solar wind velocity, *Kp* and *AE* indices showed decreases, while solar wind dynamics pressure and *Dst* index did not vary significantly. The boundaries of the outer and inner radiation belts were identified by using the background counts at all energy channels as a proxy. The obtained L-MLT distribution of boundaries reflected the general structure of the radiation belts. Time-dependent L locations of the boundaries show

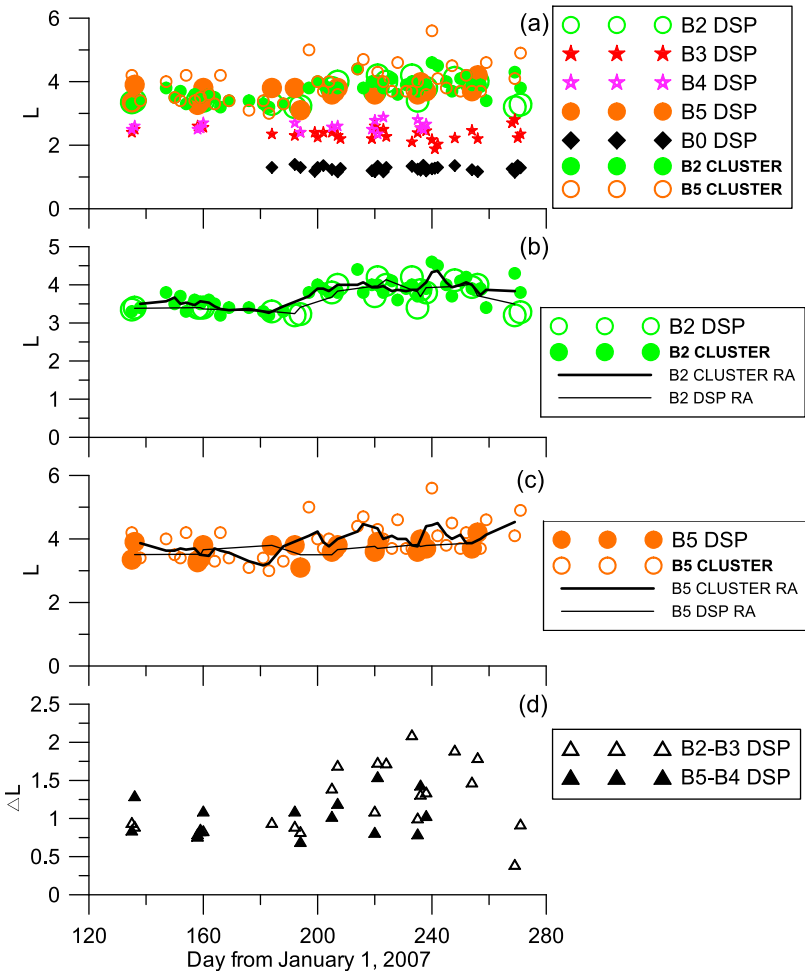

Figure 11. (a) Time-dependent L locations of all identified by Double Star boundaries: outer boundaries of the inner belt B3 (red stars) and B4 (magenta open stars), inner boundary of the inner belt B0 (black diamonds), inner boundaries of the outer belt B2 (open green circles) and B5 (orange circles). Similar boundaries identified on Cluster are B2 (green circles) and B5 (orange open circles). (b) B2 and (c) B5 boundaries from Cluster and Double Star together with running averages, (d) evolution of the slot thickness ΔL, computed similarly to Figure 10b.

no long-term correlations with variations in solar wind parameters and geomagnetic indices, however, closer examination look revealed several dips in the outer boundary location, which moved to lower L-shells (from L = 6 to L = 4). These dropouts were studied in more detail.

[58] The location and thickness of the slot region were studied using the determined inner boundaries of the outer belt and the outer boundaries of the inner belt. The slot width increased from 1.5 to 3 R_E during the end of the analyzed period, from November 2008 to January 2009. During part of the year 2007, similar boundaries of outer and/or inner radiation belts were identified in Double Star HIA spectrograms on perigee passes. It was found that the locations of the inner boundaries of the outer belt detected simultaneously by Cluster and Double Star are quite close, with difference in mean L values being 0.1.

[59] The data used in the present study do not contain direct measurements of radiation belts fluxes and do not show the exact energies/species of particles that produced measurement background. We can assume that the measured background comes from energetic MeV electrons and protons and some secondary gamma-rays produced by >100 keV electrons. Knowing the shielding parameters of the instruments, we can only estimate the energies of particles contributing to the background counts. For radiation belts' electrons, we estimate that the measured background comes from the particles, which have energies above 2 MeV. The inner radiation belt is dominated by protons with energies of tens of MeVs, whose fluxes can significantly exceed those of electrons, and the background coming from MeV protons can not be negligible compared to the electron background. The inner belt boundaries B3 and B4 mark the appearance of the background from both electrons and protons with estimated low threshold energy for the proton background as 30 MeV. The bremsstrahlung-produced gamma-rays from the energetic electrons with energies around and above 100 keV can also penetrate the detector and contribute to the measured background.

[60] The obtained locations of boundaries measured by two different satellites Cluster and Double Star with similar

instruments and their close coincidence imply that the method of determining the boundaries is reasonable. Thus, the data containing the indirect effects from the presence of the energetic radiation belts particles are of a great value too. It should be noted that the boundaries from Cluster and Double star are not expected to be exactly coincident, and one of the reasons for that can be the different energy threshold of the instruments. They are located at reasonable L-shells, which proves that the method of determining the boundaries is reliable, when we find similar results using different satellites with similar instruments but still with different threshold.

[61] The detailed analysis of the variations of the outer boundary of the outer belt revealed the time periods, when the boundary moved Earthward as close as L = 4. This shift can be related to increases in the solar wind dynamic pressure (4–8 nPa), which was observed right before the flux dropouts. This relation was mentioned by *Shprits et al.* [2006], although observations of only two storms were presented there. Most recently *Morley et al.* [2010] performed statistical analysis of the outer radiation belt flux dropout. The flux dropouts possibly occur due to losses to the magnetopause and outward diffusion.

[62] Although the variations of the outer boundary of the outer belt can be not only due to the dynamics of MeV electrons but also 100 keV electrons producing gamma-rays, which contribute to the measured background, we discuss the observed flux dropouts in terms of MeV electron component. Losses to the magnetopause assisted by the Dst effect [e.g., *Kim et al.*, 2010] will deplete the electron phase space density (PSD) in the outer regions of the radiation belts. This loss in the outer region will create inward gradients in the PSD that will drive the outward radial diffusion. There are two effects associated with the outward radial diffusion, both of them act to produce the earthward shift of the outer boundary. First, particles will loose energy as they diffuse outwards into the regions of the weaker magnetic field conserving the first and the second adiabatic invariants. Second loss effect is associated with the additional loss of electrons to the magnetopause due to the outward diffusion. Electrons from the inner regions will preferentially diffuse outward, when the PSD gradient is negative. That will act to decrease fluxes in the inner region. Electrons that were transported outward by the outward diffusion may find themselves on the drifting orbits that cross the magnetopause. This effect will create additional loss of elections from the system and will deplete electron fluxes in the inner region at lower L-shells. Another interesting feature is that the outer boundary of the outer belt moves outward after being shifted to L = 4. During the declining phase of the solar cycle, magnetic storms are caused by CIR (corotating interaction regions) with HSS. Increase in V_{sw} can indicate a HSS (Figure 7), and a small storm can occur. An increase in *Kp* can cause an increase in electric field and enhanced convection, resulting in more seed population coming from the plasma sheet. An *AE* increase indicates the presence of substorm activity, so the seed population from the plasma sheet is transported and accelerated. At the same time, the period is still quiet and the plasmapause is at large L-shells. The position of boundary can depend on the balance between particle losses and incoming/accelerated particles.

[63] The slot region is formed, as is generally known, by the losses of energetic electrons due to enhanced pitch angle scattering by VLF waves, mainly whistler waves associated with plasmaspheric hiss emission. In our present analysis the slot region defined as a region between the disappearance of the measured background inside the outer belt and the appearance of the background when entering the inner belt, so the measured background contains the contributions from the energetic protons in the inner belt. Nevertheless, we discuss the slot dynamics in terms of losses of energetic electrons. The observed slot region was found widening in the beginning of the year 2009. The year 2009 was very quiet, which was reflected in very weak radiation belts or even disappearance, as measured on board SAMPEX satellite (D. Baker, Cluster 10th Anniversary Workshop, Corfu, Greece, Sept. 2010). During weak geomagnetic activity the ULF waves due to buffeting of the magnetosphere by P_{sw}, which drives the inward radial diffusion, are weak. ULF waves that may be produced by Kelvin-Helmholz instability are also weak since solar wind velocity is weak. Similarly, waves produced by convective injections of protons should be weak during the times of weak vB_z. Plasmapause, which extends to higher L-shells will further weaken ULF activity since plasmapause may reflect ULF waves [*Hartinger et al.*, 2010]. Consequently, inward radial transport is also weak. The same weak activity is observed for chorus waves, which do not occur inside the plasmasphere that expands to higher L-shells during quiet times. Inside the plasmasphere, where the ratio between plasma and gyrofrequencies is high, local acceleration is inefficient and can not produce significant energization of electrons.

[64] Keeping the above in mind, the conclusions are the following:

[65] 1. Boundaries of radiation belts determined from background measurements on the instruments with energy ranges that do not cover the radiation belts' energies provide valuable additional information that is useful for radiation belts' model development and validation.

[66] 2. Solar wind pressure increases are important for the Earthward shift of the outer boundary of the outer belt.

[67] 3. During intervals of low activity in the solar wind parameters, the slot region widens, which is consistent with weaker inward radial diffusion and weak local acceleration that can occur only at higher L-shells outside the plasmasphere.

[68] **Acknowledgments.** The authors gratefully acknowledge the support of this work by Observatoire Midi-Pyrénées (poste rouge to N. Ganushkina). We thank OMNIWEB data center for IMF and solar wind parameter data, World Data Center C2 for Geomagnetism, Kyoto, for the provisional *AE*, *Kp*, and *Dst* indices data. We acknowledge CAA and the RAPID team for the RAPID data. N. Ganushkina's work was partly supported by the Academy of Finland. Y. Shprits would like to acknowledge the support from AFOSR grant FA9550-08-1-0140 and UC grant 09-LR-04-11672-SHPY. The authors are very grateful to D. Boscher for helpful discussions and comments.

[69] Masaki Fujimoto thanks Josef Koller and another reviewer for their assistance in evaluating this paper.

References

Abel, B., and R. Thorne (1998), Electron scattering loss in Earth's inner magnetosphere: 1. Dominant physical processes, *J. Geophys. Res.*, *103*(A2), 2385–2396.

Baker, D. N., S. G. Kanekal, T. I. Pulkkinen, and J. B. Blake (1994), Equinoctial and solstitial averages of magnetospheric relativistic electrons: A strong semiannual modulation, *Geophys. Res. Lett.*, *26*, 3193–3196.

Baker, D. N., S. G. Kanekal, X. Li, S. P. Monk, J. Goldstein, and J. L. Burch (2004), An extreme distortion of the Van Allen belt arising from the Halloween solar storm in 2003, *Nature*, *432*, 878–881, doi:10.1038/nature03116.

Balogh, A., et al. (2001), The Cluster magnetic field investigation: Overview of in-flight performance and initial results, *Ann. Geophys.*, *19*, 1207–1217.

Boscher, D., and S. Bourdarie (2001), Modeling the radiation belts: What are the important physical processes to be taken into account in models?, *Adv. Space Res.*, *28*(12), 1739–1746.

Carr, C., et al. (2005), The Double Star magnetic field investigation: Instrument design, performance and highlights of the first year's observations, *Ann. Geophys.*, *23*, 2713–2732.

Chen, Y., R. H. W. Friedel, and G. D. Reeves (2006), Phase space density distributions of energetic electrons in the outer radiation belt during two Geospace Environment Modeling Inner Magnetosphere/Storms selected storms, *J. Geophys. Res.*, *111*, A11S04, doi:10.1029/2006JA011703.

Dandouras, I., et al. (2005), Multipoint observations of ionic structures in the plasmasphere by CLUSTER-CIS and comparisons with IMAGE-EUV observations and with model simulations, in *Inner Magnetosphere Interactions: New Perspectives From Imaging*, *Geophys. Monogr. Ser.*, vol. 159, edited by J. Burch, M. Schulz, and H. Spence, pp. 23–53, AGU, Washington, D. C.

Dandouras, I., J. Cao, and C. Vallat (2009), Energetic ion dynamics of the inner magnetosphere revealed in coordinated Cluster-Double Star observations, *J. Geophys. Res.*, *114*, A01S90, doi:10.1029/2007JA012757.

Dessler, A., and R. Karplus (1961), Some effects of diamagnetic ring currents on Van Allen radiation, *J. Geophys. Res.*, *66*, 2289–2295.

Drouin, D., A. R. Couture, D. Joly, X. Tastet, V. Aimez, and R. Gauvin (2007), CASINO V2.42: A fast and easy-to-use modeling tool for scanning electron microscopy and microanalysis users, *Scanning*, *29*, 92–101.

Escoubet, C. P., M. Fehringer, and M. Goldstein (2001), The Cluster mission, *Ann. Geophys.*, *19*, 1197–1200.

Friedel, R. H. W., G. D. Reeves, and T. Obara (2002), Relativistic electron dynamics in the inner magnetosphere: A review, *J. Atmos. Sol. Terr. Phys.*, *64*, 265–282.

Fung, S. F., X. Shao, and L. C. Tan (2006), Long-term variations of the electron slot region and global radiation belt structure, *Geophys. Res. Lett.*, *33*, L04105, doi:10.1029/2005GL024891.

Goldstein, J., S. Kanekal, D. N. Baker, and B. R. Sandel (2005), Dynamic relationship between the outer radiation belt and the plasmapause during March–May 2001, *Geophys. Res. Lett.*, *32*, L15104, doi:10.1029/2005GL023431.

Green, J. C., and M. G. Kivelson (2004), Relativistic electrons in the outer radiation belt: Differentiating between acceleration mechanisms, *J. Geophys. Res.*, *109*, A03213, doi:10.1029/2003JA010153.

Green, J. L., S. Boardsen, L. Garcia, W. W. L. Taylor, S. F. Fung, and B. W. Reinisch (2005), On the origin of whistler mode radiation in the plasmasphere, *J. Geophys. Res.*, *110*, A03201, doi:10.1029/2004JA010495.

Hartinger, M., M. B. Moldwin, V. Angelopoulos, K. Takahashi, H. J. Singer, R. R. Anderson, Y. Nishimura, and J. R. Wygant (2010), Pc5 wave power in the quiet-time plasmasphere and trough: CRRES observations, *Geophys. Res. Lett.*, *37*, L07107, doi:10.1029/2010GL042475.

Iles, R. H. A., N. P. Meredith, A. N. Fazakerley, and R. B. Horne (2006), Phase space density analysis of the outer radiation belt energetic electron dynamics, *J. Geophys. Res.*, *111*, A03204, doi:10.1029/2005JA011206.

Imhof, W. L., et al. (1982), Coordinated measurements of slot region electron precipitation by plasmaspheric wave bands, *J. Geophys Res.*, *87*, 4418–4426.

Imhof, W. L., et al. (1986), Slot region electron precipitation by lightning, VLF chorus, and plasmaspheric hiss, *J. Geophys. Res.*, *91*, 8883–8894.

Kasahara, S., K. Asamura, K. Ogasawara, Y. Kazama, T. Takashima, M. Hirahara, and Y. Saito (2009), A noise attenuation method for medium-energy electron measurements in the radiation belt, *Adv. Space Res.*, *43*, 792–801.

Kim, H.-J., and A. A. Chan (1997), Fully adiabatic changes in storm-time relativistic electron fluxes, *J. Geophys. Res.*, *102*, 22,107–22,116.

Kim, K.-C., D.-Y. Lee, H.-J. Kim, E. S. Lee, and C. R. Choi (2010), Numerical estimates of drift loss and Dst effect for outer radiation belt relativistic electrons with arbitrary pitch angle, *J. Geophys. Res.*, *115*, A03208, doi:10.1029/2009JA014523.

Li, X., D. N. Baker, M. Temerin, T. E. Cayton, E. G. D. Reeves, R. A. Christensen, J. B. Blake, M. D. Looper, R. Nakamura, and S. G. Kanekal (1997), Multisatellite observations of the outer zone electron variation during the November 3–4, 1993, magnetic storm, *J. Geophys. Res.*, *102*, 14,123–14,140.

Li, X., D. N. Baker, S. G. Kanekal, M. Looper, and M. Temerin (2001), Long term measurements of radiation belts by SAMPEX and their variations, *Geophys. Res. Lett.*, *28*, 3827–3830.

Li, X., D. N. Baker, M. Temerin, G. D. Reeves, R. Friedel, and C. Shen (2005), Energetic electrons, 50 keV–6 MeV, at geosynchronous orbit: Their responses to solar wind variations, *Space Weather*, *3*, S04001, doi:10.1029/2004SW000105.

Li, X., D. N. Baker, T. P. O'Brien, L. Xie, and Q. G. Zong (2006), Correlation between the inner edge of outer radiation belt electrons and the innermost plasmapause location, *Geophys. Res. Lett.*, *33*, L14107, doi:10.1029/2006GL026294.

Lyons, L., and R. Thorne (1973), Equilibrium structure of radiation belt electrons, *J. Geophys. Res.*, *78*(13), 2142–2149.

Lyons, L. R., and D. J. Williams (1984), *Quantitative Aspects of Magnetospheric Physics*, 231 pp., Springer, New York.

MacDonald, E. A., M. F. Thomsen, and H. O. Funsten (2006), Background in channel electron multiplier detectors due to penetrating radiation in space, *IEEE Trans. Nucl. Sci.*, *53*, 1593–1598.

Miyoshi, Y., A. Morioka, T. Obara, H. Misawa, T. Nagai, and Y. Kasahara (2003), Rebuidling process of the outer radiation belt during the November 3, 1993 magnetic storm: NOAA and EXOS-D observations, *J. Geophys. Res.*, *108*(A1), 1004, doi:10.1029/2001JA007542.

Morley, S. K., R. H. W. Friedel, T. E. Cayton, and E. Noveroske (2010), A rapid, global and prolonged electron radiation belt dropout observed with the Global Positioning System constellation, *Geophys. Res. Lett.*, *37*, L06102, doi:10.1029/2010GL042772.

O'Brien, T. P., R. L. McPherron, D. Sornette, G. D. Reeves, R. Friedel, and H. J. Singer (2001), Which magnetic storms produce relativistic electrons at geosynchronous orbit?, *J. Geophys. Res.*, *106*, 15,533–15,544, doi:10.1029/2001JA000052.

Onsager, T. G., G. Rostoker, H. J. Kim, G. D. Reeves, T. Obara, and C. Smithtro (2002), Radiation belt electron flux dropouts: Local time, radial and particle-energy dependence, *J. Geophys. Res.*, *107*(A11), 1382, doi:10.1029/2001JA000187.

Reeves, G. D., R. H. W. Friedel, R. D. Belian, M. M. Meiet, M. G. Henderson, T. Onsager, H. J. Singer, D. N. Baker, X. Li, and J. B. Blake (1998), The relativistic electron response at geosynchronous orbit during the January 1997 magnetic storm, *J. Geophys. Res.*, *103*, 17,559–17,570.

Reeves, G. D., K. L. McAdams, R. H. W. Friedel, and T. P. O'Brien (2003), Acceleration and loss of relativistic electrons during geomagnetic storms, *Geophys. Res. Lett.*, *30*(10), 1529, doi:10.1029/2002GL016513.

Réme, H., et al. (2001), First multispacecraft ion measurements in and near the Earth's magnetosphere with the identical CLUSTER Ion Spectrometry (CIS) Experiment, *Ann. Geophys.*, *19*, 1303–1354.

Réme, H., et al. (2005), The HIA instrument onboard the Tan Ce 1 Double Star near-equatorial spacecraft and its first results, *Ann. Geophys.*, *23*, 2757–2774.

Shprits, Y. Y., R. M. Thorne, R. Friedel, G. D. Reeves, J. Fennell, D. N. Baker, and S. G. Kanekal (2006), Outward radial diffusion driven by losses at magnetopause, *J. Geophys. Res.*, *111*, A11214, doi:10.1029/2006JA011657.

Shprits, Y. Y., N. P. Meredith, and R. M. Thorne (2007), Parameterization of radiation belt electron loss timescales due to interactions with chorus waves, *Geophys. Res. Lett.*, *34*, L11110, doi:10.1029/2006GL029050.

Shprits, Y. Y., S. R. Elkington, N. P. Meredith, and D. A. Subbotin (2008a), Review of modeling of losses and sources of relativistic electrons in the outer radiation belt I: Radial transport, *J. Atmos. Sol. Terr. Phys.*, *70*(14), 1679–1693.

Shprits, Y. Y., D. A. Subbotin, N. P. Meredith, and S. R. Elkington (2008b), Review of modeling of losses and sources of relativistic electrons in the outer radiation belt II: Local acceleration and loss, *J. Atmos. Sol. Terr. Phys.*, *70*(14), 1694–1713.

Thorne, R. M., E. J. Smith, K. J. Fiske, and S. R. Church (1974), Intensity variation of ELF hiss and chorus during isolated substorms, *Geophys. Res. Lett.*, *1*(5), 193–196.

Thorne, R. M., Y. Y. Shprits, N. P. Meredith, R. B. Horne, W. Li, and L. R. Lyons (2007), Refilling of the slot region between the inner and outer electron radiation belts during geomagnetic storms, *J. Geophys. Res.*, *112*, A06203, doi:10.1029/2006JA012176.

Tsyganenko, N. A. (1989), A magnetospheric magnetic field model with a warped tail current sheet, *Planet. Space Sci.*, *37*, 5–20.

Tverskaya, L. V., N. N. Pavlov, J. B. Blake, R. S. Selesnick, and J. F. Fennell (2003), Predicting the L-position of the storm-injected relativistic electron belt, *Adv. Space Res.*, *31*(4), 1039–1044.

Vallat, C., I. Dandouras, M. Dunlop, A. Balogh, E. Lucek, G. K. Parks, M. Wilber, E. C. Roelof, G. Chanteur, and H. Réme (2005), First current

density measurements in the ring current region using simultaneous multispacecraft CLUSTER-FGM data, *Ann. Geophys.*, *23*, 1849–1865.

Vallat, C., N. Ganushkina, I. Dandouras, C. P. Escoubet, M. Taylor, H. Laakso, A. Masson, J.-A. Sauvaud, H. Réme, and P. Daly (2007), Ion multi-nose structures observed by Cluster in the inner magnetosphere, *Ann. Geophys.*, *25*, 171–190.

Wilken, B., et al. (1997), RAPID-The Imaging energetic particle spectrometer on Cluster, *Space Sci. Rev.*, *79*, 399–473.

Zheng, Y., A. T. Y. Lui, X. Li, and M.-C. Fok (2006), Characteristics of 2–6 MeV electrons in the slot region and inner radiation belt, *J. Geophys. Res.*, *111*, A10204, doi:10.1029/2006JA011748.

Ziegler, J. F., M. D. Ziegler, and J. P. Biersack (2010), SRIM- The stopping and range of ions in matter, *Nucl. Instrum. Methods Phys. Res., Sect. B*, *268*, 1818–1823.

J. Cao, School of Astronautics, Beijing University of Aeronautics and Astronautics, Beijing 100190, China.

I. Dandouras, IRAP, UPS-OMP, University of Toulouse, CNRS, 9 Av. Colonel Roche, BP 44346, F-31028 Toulouse CEDEX 4, France.

N. Y. Ganushkina, Department of Atmospheric, Oceanic and Space Sciences, University of Michigan, 2455 Hayward St., Ann Arbor, MI 48109-2143, USA. (ganuna@umich.edu)

Y. Y. Shprits, Institute of Geophysics and Planetary Physics, Department of Atmospheric and Oceanic Sciences, 7127 Math Sciences Bldg., 405 Hilgard Ave., Los Angeles, CA 90095-1565, USA.